Effect of redox conditions on the structure and solubility of sulfur- and selenium-AFm phases

Latina Nedyalkova[a,b,*], Barbara Lothenbach[a], Guillaume Renaudin[c], Urs Mäder[d], Jan Tits[b]

[a)] Laboratory for Concrete and Construction Chemistry, Empa, Dübendorf, Switzerland

[b)] Laboratory for Waste Management, Paul Scherrer Institute, Villigen PSI, Switzerland

[c)] Université Clermont Auvergne, CNRS, SIGMA Clermont, ICCF, F-63000 Clermont-Ferrand, France

[d)] Institute of Geological Sciences, University of Bern, Switzerland

* Corresponding author.

E-mail address: latina.nedyalkova@empa.ch; latina_nedyalkova@abv.bg (L. Nedyalkova)

Keywords: AFm phase, solubility (B), waste management (E), selenium, sulfur

Abstract

In the context of safe radioactive waste disposal, the incorporation of selenium and sulfur, a major competitor for Se, in AFm phases was investigated by synthesizing and characterizing Se(VI)-, Se(IV)-, S(VI)-, S(IV)-, S(II)-AFm phases to account for a range of possible redox conditions in a cement-based repository for low and intermediate level radioactive waste.

The X-ray spectra revealed crystalline AFm phases with trigonal or pseudo-trigonal structure. Different interlayer distances (hkl 00l) were observed for the phases described in the hexagonal lattice, whereas no shift of the (hkl 110) diffraction peak was detected. The type of the interlayer anion seems to control the crystal symmetry of the AFm phase. The amount of water in the interlayer depends on the interlayer anion, relative humidity and temperature of exposure. The AFm phases show similar solubility

products suggesting that high sulfur concentration in the cement pore solution can decrease Se binding by AFm phases.

1. Introduction

In blast furnace slag cements [1] and Portland cements blended with slags [2], Fe(0) and the reduced sulfur species, HS^- (S^{-II}, sulfide), from the slag lead to reducing conditions in the pore solution. Experimental investigations of the pore solution of such cements have shown that not only HS^- from the slag reaction and SO_4^{2-} (S^{VI}, sulfate) from Portland cement are present in the pore solution, but also the intermediate SO_3^{2-} (S^{IV}, sulfite) and $S_2O_3^{2-}$ (S^{II}, thiosulfate). The latter two originate from the partial oxidation of HS^- and have been observed to persist for years in the pore solution of slag containing cements [1, 2]. The binding of SO_4^{2-} in AFm (Al_2O_3-Fe_2O_3-mono) and AFt (Al_2O_3-Fe_2O_3-tri) phases is well investigated (e.g. [3]), while much less is known whether and to which extend reduced sulfur species ($S_2O_3^{2-}$, SO_3^{2-} and HS^-) can be bound in AFm or AFt phases.

Reducing conditions are not only found in the presence of blast furnace slags, but also in the near-field of deep geological repositories as foreseen in Switzerland for the disposal of low- and intermediate level nuclear waste (L/ILW), where cementitious materials will be a component of the waste matrix and will be used for the construction of the engineered barrier system [4]. Thermodynamic calculations predict an alkaline environment ($10 < pH < 13.5$) for the near field of such cement-based repositories and redox conditions evolving from an initial oxidising stage due to the residual oxygen entrapped in pore spaces, to anoxic conditions caused by the oxygen consumption by microorganisms, abiotic oxidation processes and the production of hydrogen by radiolysis. In the long term, the redox potential will range between -750 mV and -230 mV (SHE) assuming that redox conditions are mainly controlled by Fe(III)/Fe(II) mineral equilibria [5].

One of the dose-determining radionuclides potentially emanating from L/ILW repositories is considered to be selenium-79 due to its long half-life ($t_{1/2}$ ~3.27 x 10^5 a) and expected weak retention by

many common near- and far-field minerals as a result of its anionic speciation [4]. During the evolution of the redox conditions in the repository, several oxidation states of Se may occur and its aqueous speciation will be dominated by SeO_4^{2-} (Se^{VI}, selenate) and SeO_3^{2-} (Se^{IV}, selenite ion) under oxidizing conditions; HSe^- (Se^{-II}, selenide) and a series of polyselenides (Se_x^{2-}, x=2,3,4) under reducing conditions [6] (Fig. 1a). Depending on the composition of the cementitious matrix and the redox conditions, different anionic sulfur species, namely SO_4^{2-} (S^{VI}, sulfate), SO_3^{2-} (S^{IV}, sulfite), $S_2O_3^{2-}$ (S^{II}, thiosulfate) and HS^- (S^{-II}, sulfide), may also be present. The sulfur anions are isostructural with the selenium ones and have similar chemical properties. Thus, a strong influence of sulfur on the selenium binding is expected. SO_3^{2-} and $S_2O_3^{2-}$ are thermodynamically metastable relative to the main species SO_4^{2-} and HS^- (Fig. 1b and 1c). Reduced sulfur species (HS^-, SO_3^{2-} and $S_2O_3^{2-}$), however, are observed to persist in pore solutions of blast furnace slag cement due to slow oxidation kinetics [1, 7].

A potential retardation mechanism for the hazardous Se anions is their uptake by positively charged anion exchangers, such as AFm phases, present in the cementitious near-field. AFm (Al_2O_3-Fe_2O_3-mono) phases are calcium aluminate-ferrite hydrates belonging to the layered double hydroxide (LDH) family. They are formed during the hydration of cement and have the general formula $[Ca_4(Al,Fe)_2(OH)_{12}]\cdot X\cdot nH_2O$ where X stands for either two monovalent anions or a bivalent anion. The structure is composed of positively charged main layers, $[Ca_4(Al,Fe)_2(OH)_{12}]^{2+}$, and negatively charged interlayers, $[X\cdot nH_2O]^{2-}$, with n giving the number of interlayer water molecules. The amount of water in the interlayer varies depending on the type of interlayer anion, the temperature and the relative humidity [8]. Although the most common interlayer anions found in the AFm are OH^-, SO_4^{2-}, Cl^- and CO_3^{2-} [3, 9], a variety of other anions can be incorporated as well in the AFm structure, such as NO_3^- [10], I^- [11], Br^- [12], CrO_4^{2-} [13, 14], or MoO_4^{2-} [15]. Bi-anionic AFm phases, containing more than one type of interlayer anion, may also form and have been reported in literature [11, 16-20]. Thus AFm phases may provide a large potential for the immobilization of the Se anions due to these interlayer anion exchange sites.

The ability of the AFm phases to bind Se has already been studied before, but a more comprehensive understanding of the sorption mechanism as well as of the effect of the competition with S is still needed. Several studies so far have focused on the formation of Se-AFm and S-AFm phases. Se(VI)-, Se(IV)- and Se(-II)-AFm have been synthesized (e.g. [21-24]) but their crystal structure has not yet been resolved. The formation of the S(VI)-AFm (monosulfate), on the other hand, has been extensively studied and its structure refined in the rhombohedral $R\bar{3}$ space group [25]. Monosulfate is known to exist in several hydration states - Ms9, Ms10.5, Ms12 and Ms14 (with the index number giving the water content of the phase per unit cell in moles), in dependence of the exposure temperature and relative humidity. As the water molecules are incorporated in the interlayer, each hydrate has a specific interlayer distance [26, 27]. The S(IV)-AFm [28] and the S(-II)-AFm [29] phases have been synthesized and their crystal structure characterized revealing a rhombohedral structure for both phases, but no solubility measurements have been performed. The existence of a S(II)-AFm phase has been suggested previously [30], however, it has not yet been synthesized.

This study aims to extend the current knowledge on the incorporation of Se and S in AFm phases by gaining a better insight into the crystal structure, hydration states and solubility of the various Se-AFm and S-AFm phases and also to consider the effect of competition between these chemically similar elements for the available AFm sites. Se(VI)-, Se(IV)-, S(VI)-, S(IV)-, S(II)-AFm phases were synthesized and investigated with the aim of accounting for a range of possible redox conditions in a cement-based repository. Due to the difficulties related to the stabilization of the strongly reduced Se(-II) and S(-II) anionic species and the different techniques required for their synthesis and characterization, AFm phases containing these anions were not included.

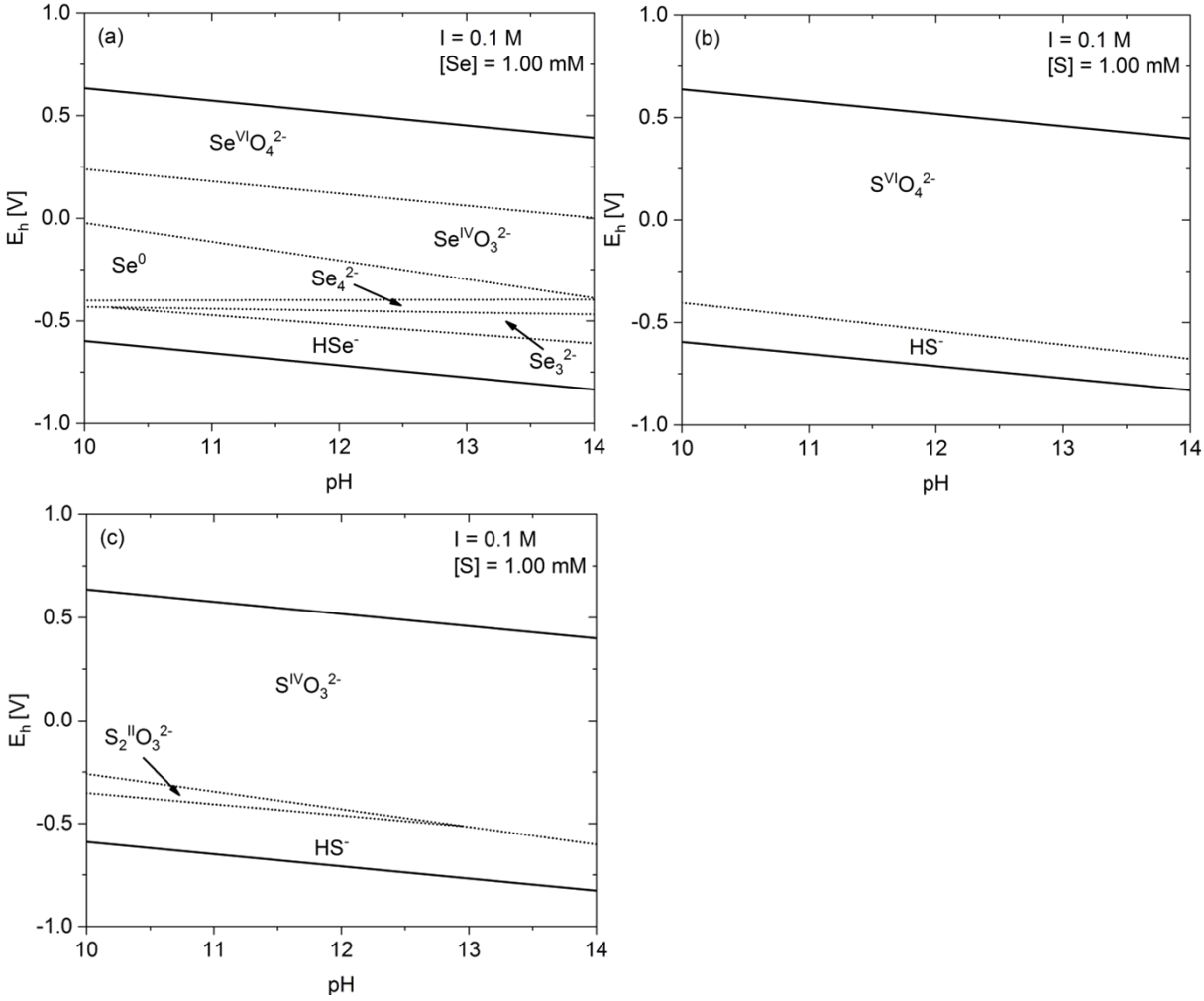

Figure 1: Predominance diagrams for selenium (a) and sulfur (b); Eh-pH diagram for the metastable sulfur species SO_3^{2-} and $S_2O_3^{2-}$ (c). Calculations were performed using the Medusa code [31] and thermodynamic data from the NEA thermodynamic database [32].

2. Materials and Methods

2.1 Synthesis of AFm phases

All sample manipulations were performed in a N_2-filled glove box to minimize atmospheric CO_2 contamination. Solutions were prepared using high-purity deionized water (resistivity = 18.2 MΩ cm) generated by a Milli-Q Gradient A10 System (Millipore, Bedford, USA). All chemicals were analytical grade reagents. The following chemicals were used: CaO, $CaCO_3$, Al_2O_3, Na_2SO_4, Na_2SO_3, $Na_2S_2O_3{\cdot}5H_2O$,

119 Na_2SeO_4, $Na_2SeO_3 \cdot 5H_2O$, $CaSO_4 \cdot 2H_2O$ (Sigma-Aldrich, St. Louis, Missouri, USA) and $CaSeO_3$ (American
120 Elements, Los Angeles, California, USA). Tricalcium aluminate (C_3A) was prepared by mixing appropri-
121 ate amounts of $CaCO_3$ with Al_2O_3 powder to achieve a molar ratio of 3:1 and by heating the mixture at
122 800°C for 1h, at 1000°C for another 4h and finally at 1425°C for 24 h. The clinkers were then ground to
123 <63 µm. The powder was checked by X-ray diffraction to confirm the formation of cubic C_3A (PDF: 00-
124 038-1429). To ensure that no CO_2 contamination of CaO occurred, the latter compound was heated at
125 900°C for 12 h prior to the start of the synthesis. All Na- and Ca-salts were tested for the presence of
126 absorbed H_2O by thermogravimetric analysis (TGA) to determine their actual composition.

127 The AFm phases were synthesized by mixing approximately 2 g of the starting materials C_3A, CaO, and
128 the appropriate Na_2-X salt in stoichiometric amounts (in 1:1:1 molar ratio) in 50 ml of ultrapure water
129 resulting in a Na concentration of 0.2 M and pH of ~13. The S(VI)-AFm and Se(IV)-AFm phases were al-
130 so prepared at pH~12 using Ca-X salts. For the S(IV)-, S(II)- and Se(VI)-AFm no Ca-X salts were com-
131 mercially available.

132 The samples were equilibrated for three or six months, in closed PE-bottles at 20°C on end-over-end
133 shakers (100 rpm). After equilibration, the solid and liquid phases were separated by vacuum filtration
134 through a 0.45 µm nylon filter. The solid phases were dried in a desiccator over a saturated NaOH so-
135 lution (~8 % relative humidity) at room temperature for five to six weeks under vacuum.

136

137

138 ## 2.2 Characterization of the solid phases

139 After drying, the samples were analysed by X-ray powder diffraction (XRPD), thermogravimetric analy-
140 sis (TGA), infrared (FTIR) and Raman spectroscopy, and dynamic vapour sorption (DVS).

141 XRPD analyses were performed on a PANalytical X'Pert Pro MPD diffractometer using CuKα radiation
142 (λ = 1.54184 Å); the diffraction patterns were recorded between $5 < 2\theta < 70°$ with a step size of 0.017°
143 (2θ) and a counting time of 0.6 s per step. For the Rietveld refinement, XRPD patterns were recorded
144 on a PANalytical X'Pert Pro diffractometer with θ-θ geometry, equipped with a solid X-Celerator detec-

145 tor and using CuKα radiation. XRPD patterns were recorded at room temperature in the interval 3° <
146 2θ < 120°, with a step size of 0.0167° and a counting time of 2 s for each data value. A total counting
147 time of about 200 min was used for each sample. An attempt to solve the crystal structures of the AFm
148 phases was done using X-Cell software to determine the unit cell symmetry [33], FOX software to lo-
149 cate the unit cell objects [34] and, finally, structure refinement was done by the Rietveld method with
150 the FULLPROF software [35].

151 TGA was carried out on a TGA/SDTA 851 instrument (Mettler Toledo, Switzerland). The samples (~15
152 mg) were heated under a N_2 atmosphere over the temperature range between 30 and 980°C at a heat-
153 ing rate of 20°C/min. The obtained mass losses were then used to determine the water content of the
154 solids. In order to characterize the different functional groups and the type of structurally bound water
155 (OH or H_2O) of the AFm phases, attenuated total reflectance infrared spectra were recorded in the
156 4000 to 600 cm^{-1} range on a Bruker Tensor 27 FTIR spectrometer. Raman spectroscopy measurements
157 were carried out on a Raman Bruker Senterra instrument using a 532 nm laser and a 3.5 cm^{-1} spectral
158 resolution to determine the vibrational characteristics of the molecules in the structure.

159 The water sorption kinetics of the samples were studied with a VTI-SA Dynamic Vapour Sorption (DVS)
160 apparatus (TA Inc, USA). The relative humidity (RH) was varied between 5, 10, 20, 30, 50, 60, 70, 80, 85,
161 90, 92, 94, 90, 80, 70, 50, 30, 20, 10, and 5 % at 25°C with a data logging interval of 1 min. The equilib-
162 rium criterion for each RH step was set to 0.0065 wt. % of the sample mass in 5 min for a maximum
163 equilibration time of 720 min; equilibrium was reached for all samples within the maximum equilibra-
164 tion time. The reference mass was obtained by drying the sample at 105°C and 0% RH.

165

166

167 2.3 Characterization of the liquid phases

168 Immediately after filtration, the pH was measured using a Knick pH-meter with a SE 100 pH/Pt 1000
169 electrode (Knick, Germany) at room temperature. The electrode was calibrated with NaOH solutions of
170 known concentrations. The chemical composition of the liquid phases was analysed with a Dionex ICS-

171 3000 ion chromatography system equipped with a Dionex Ion Pac AS25 column for SO_4, SO_3, S_2O_3,
172 SeO_4 and SeO_3; a Dionex Ion Pac CS12A column for Na and Ca; and a Dionex Ion Pac CS5A column for
173 Al. The eluents used were 37 ml of 1.0 M NaOH/1 l water for the anions, 1.3 ml of ≥99.5% methanesul-
174 fonic acid (MSA)/1 l water for Na and Ca, and 74 ml of 32% HCl/1 l water for Al, respectively. The dis-
175 solved Al and S_2O_3 concentrations were quantified in the undiluted solutions; for the other elements
176 the samples were diluted by a factor of 1:10 in the case of SO_4, SO_3, SeO_4 and SeO_3; and 1:100 in the
177 case of Na (and Ca in the case of the pH~12 samples).

178

179

180 ### 2.4 Experimental and analytical challenges

181 Sulfite oxidation: In dilute alkaline solutions, it was observed that sulfite was unstable outside of the
182 N_2-filled glovebox and tended to oxidize slowly to sulfate. To stabilize sulfite for the IC measurements,
183 the IC standards and sample dilutions were prepared in the glovebox where 100 µl of formaldehyde
184 solution (in a 1:1000 dilution) were added to 10 ml aliquot of each standard and sample. A small por-
185 tion of the sulfite in solution, however, still oxidized and the IC results had to be corrected. The data
186 were corrected by subtracting the SO_4 concentration from the total S concentration of the IC standards
187 and attributing the remaining portion to SO_3. The SO_3 concentration obtained in this manner was then
188 plotted against the measured SO_3 peak area resulting in a linear relationship used to correct all further
189 measurements. For some samples, the quality of the correction was controlled by ICP-OES measure-
190 ments. In the thiosulfate samples no oxidation was observed.

191

192

193 ### 2.5 Calculation of thermodynamic data

194 The measured concentrations of calcium, sodium, aluminium, sulfur and selenium in the liquid phase in
195 equilibrium with the solids were used to calculate the solubility products of the synthesized AFm phas-
196 es by using the thermodynamic modelling program GEMS [36] and the NAGRA/PSI database [37], in-

cluding a full speciation calculation. The activity coefficients of the aqueous species were calculated with the built-in extended Debye-Hückel equation and NaOH as a background electrolyte. The solubility products refer to Ca^{2+}, AlO_2^-, OH^-, H_2O, SO_4^{2-}, SO_3^{2-}, $S_2O_3^{2-}$, SeO_4^{2-} and SeO_3^{2-}, respectively and solids with 4 Ca within the main layer (eg. K_{s0}(S(VI)-AFm) = $\{Ca^{2+}\}^4$ $\{AlO_2^-\}^2$ $\{SO_4^{2-}\}$ $\{OH^-\}^4$ $\{H_2O\}^{12}$ for Ms14). From the calculated solubility products also the Gibbs free energy of formation for each phase was calculated. The entropy S and the heat capacity C^0_p of monosulfate with different hydration states has been determined experimentally [27] while for $3CaO{\cdot}Al_2O_3{\cdot}CaSO_3{\cdot}11H_2O$, $3CaO{\cdot}Al_2O_3{\cdot}CaS_2O_3{\cdot}13H_2O$, $3CaO{\cdot}Al_2O_3{\cdot}CaSeO_4{\cdot}13H_2O$ and $3CaO{\cdot}Al_2O_3{\cdot}CaSeO_3{\cdot}11H_2O$ no measured data are available. The entropy and heat capacities values were thus estimated based on the following reference reactions using $3CaO{\cdot}Al_2O_3{\cdot}CaSO_4{\cdot}12H_2O$ [27]:

$$3CaO{\cdot}Al_2O_3{\cdot}CaSO_3{\cdot}11H_2O \Leftrightarrow 3CaO{\cdot}Al_2O_3{\cdot}CaSO_4{\cdot}12H_2O - H_2O - SO_4^{2-} + SO_3^{2-}$$

$$3CaO{\cdot}Al_2O_3{\cdot}CaS_2O_3{\cdot}13H_2O \Leftrightarrow 3CaO{\cdot}Al_2O_3{\cdot}CaSO_4{\cdot}12H_2O + H_2O - SO_4^{2-} + S_2O_3^{2-}$$

$$3CaO{\cdot}Al_2O_3{\cdot}CaSeO_4{\cdot}13H_2O \Leftrightarrow 3CaO{\cdot}Al_2O_3{\cdot}CaSO_4{\cdot}12H_2O + H_2O - SO_4^{2-} + SeO_4^{2-}$$

$$3CaO{\cdot}Al_2O_3{\cdot}CaSeO_3{\cdot}11H_2O \Leftrightarrow 3CaO{\cdot}Al_2O_3{\cdot}CaSO_4{\cdot}12H_2O - H_2O - SO_4^{2-} + SeO_3^{2-}$$

Selecting an isocoulombic reaction as the model reaction, in which the exchange of anions of same charge takes place, allowed to assume that the ΔC_p and ΔS terms are close to zero [38]. The entropy and heat capacity of SO_4^{2-}, SO_3^{2-}, $S_2O_3^{2-}$, SeO_4^{2-}, SeO_3^{2-}, and H_2O were taken from the GEMS Nagra/PSI thermodynamic database [37].

3. Results and discussion

3.1. X-ray diffraction patterns

The synthesized phases were characterized by XRPD. Crystal structure solution and refinement were attempted for the S(IV)-, S(II)-, Se(VI)- and Se(IV)-AFm samples. The structure of the S(VI)-AFm phase was refined by Allmann [25] and the phase is used as a reference. The XRD analyses revealed well-

222 crystalline AFm phases showing high-intensity basal reflexions (hkl 00l) at low 2θ values and the (110)
223 diffraction peak of the basal plane at ~31° 2θ characteristic for the AFm family.
224
225
226 3.1.1 S(VI)-AFm: The XRPD patterns of the S(VI)-AFm samples synthesized at pH~13 and pH
227 ~12 (Fig. 2) show no apparent effect of pH on the synthesized products. Both samples are character-
228 ized by a main diffraction peak at 9.9° 2θ corresponding to an interlayer distance of 8.93 Å and a S(VI)-
229 AFm with 12 water molecules (Ms12) after drying [27]. In the pH~13 sample a small reflection at 9.3°
230 2θ indicates the presence of minor S(VI)-AFm hydrate with 14 water molecules and an interlayer dis-
231 tance of 9.50 Å (Ms14). The water rich phase is a remnant of the saturated conditions prior to drying as
232 Ms14 is the stable hydration state at 100 % RH and temperatures above 18°C, and it dehydrates to
233 Ms12 at 97 % RH [27]. The lower pH sample shows some hemicarbonate ($Ca_4Al_2(CO_3)_{0.5}(OH)_{13}\cdot 5.5\ H_2O$
234 [20]) indicating slight carbonation. In addition, both samples contain minor ettringite
235 ($Ca_6Al_2OH_{12}(SO_4)_3\cdot 26H_2O$ [39]) impurities.
236
237
238
239
240
241
242
243
244
245

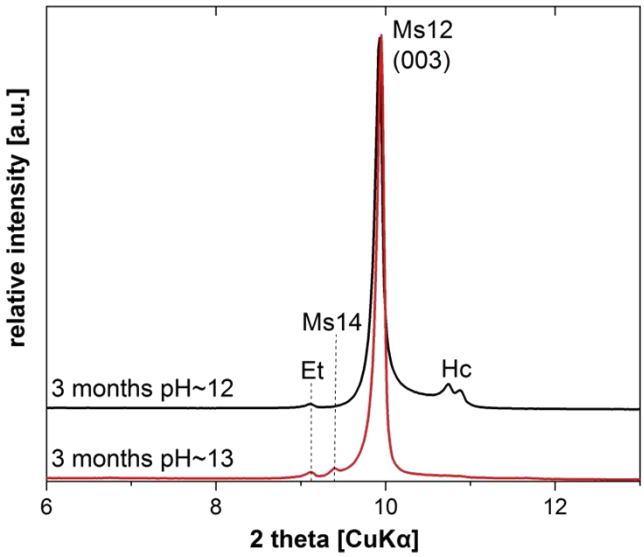

Figure 2: XRPD pattern for the S(VI)-AFm phases synthesized at pH~13 and pH~12. The samples were dried over a saturated NaOH-solution (RH ~8 %). Et: ettringite, Hc: hemicarbonate, Ms12: monosulfate with 12 H_2O molecules, Ms14: monosulfate with 14 H_2O molecules.

3.1.2 S(IV)-AFm: The analysed sample shows good crystallinity and consists of an almost single AFm phase containing only minor impurities of portlandite ($Ca(OH)_2$) (Fig. 3). The first diffraction peak at ~10.4° 2θ has a right shoulder indicating most probably the presence of small amounts of a less hydrated AFm phase or a lowering of symmetry. Nevertheless, for the crystal structure refinement data have been treated by considering a single AFm phase sample with hexagonal unit cell, thus omitting the shoulder and its harmonics. The portlandite impurities, however, were taken into account for the refinement.

The diffraction peak positions correspond to a hexagonal lattice with a rhombohedral $R\bar{3}$ space group. The refined lattice parameters are a = 5.7693(6) Å and c = 25.533(3) Å indicating an interlayer distance of 8.51 Å. The intercalated anion respects the geometrical feature of pyramidal sulfite with a S-O distance of 1.51 Å and a O-S-O angle of 106°. Two distinct structure solutions can be found with either the sulfite SO_3^{2-} anion normal to the main layer and connected to calcium cation, or parallel to

the main layer at the center of the interlayer region. These two different configurations result in similar Rietveld agreement factors, due to the difficulty to correctly model the diffraction peak shape. Nevertheless, the comparison with previously determined equivalent crystal structure from single data allow us to favour the parallel orientation. The crystal structure of the NO_3-AFm phase is characterized by planar trigonal NO_3^- anion perpendicular to the main layer (bonded to Ca^{2+}) resulting in a larger interlayer distance of 8.62 Å (even though the N-O bond distance of 1.22 Å is shorter than the S-O distance of about 1.51 Å) [10]. Then the smaller interlayer distance of the S(IV)-AFm suggests a sulfite orientation parallel to the main layer. The comparison with the HBO_3-AFm, in which the planar triangular anion is parallel to the main layer in the center of the interlayer region resulting in an interlayer distance of 8.26 Å [40], also supports the idea of the parallel central interlayer position. Complementary observations, namely by the preparation of single crystals, are needed to definitively confirm this orientation. The structural parameters assuming a parallel central interlayer position described in the rhombohedral $R\bar{3}$ space group are summarized in Table 1, and Figure 3 shows the corresponding Rietveld plot. The refined composition corresponds to $[Ca_2Al(OH)_6]\cdot[½SO_3\cdot2.1H_2O]$, or $3CaO\cdot Al_2O_3\cdot CaSO_3\cdot10.2H_2O$, slightly below the obtained 11 water molecules per formula unit determined by the chemical analysis (see chapter 3.2.1).

Motzet & Pöllmann [28] assigned the S(IV)-AFm unit cell to the trigonal space groups $P3$ or $P\bar{3}$ with the refined lattice parameters a = 5.7709(4) Å and c = 51.284(5) Å (twice the unit cell used here).

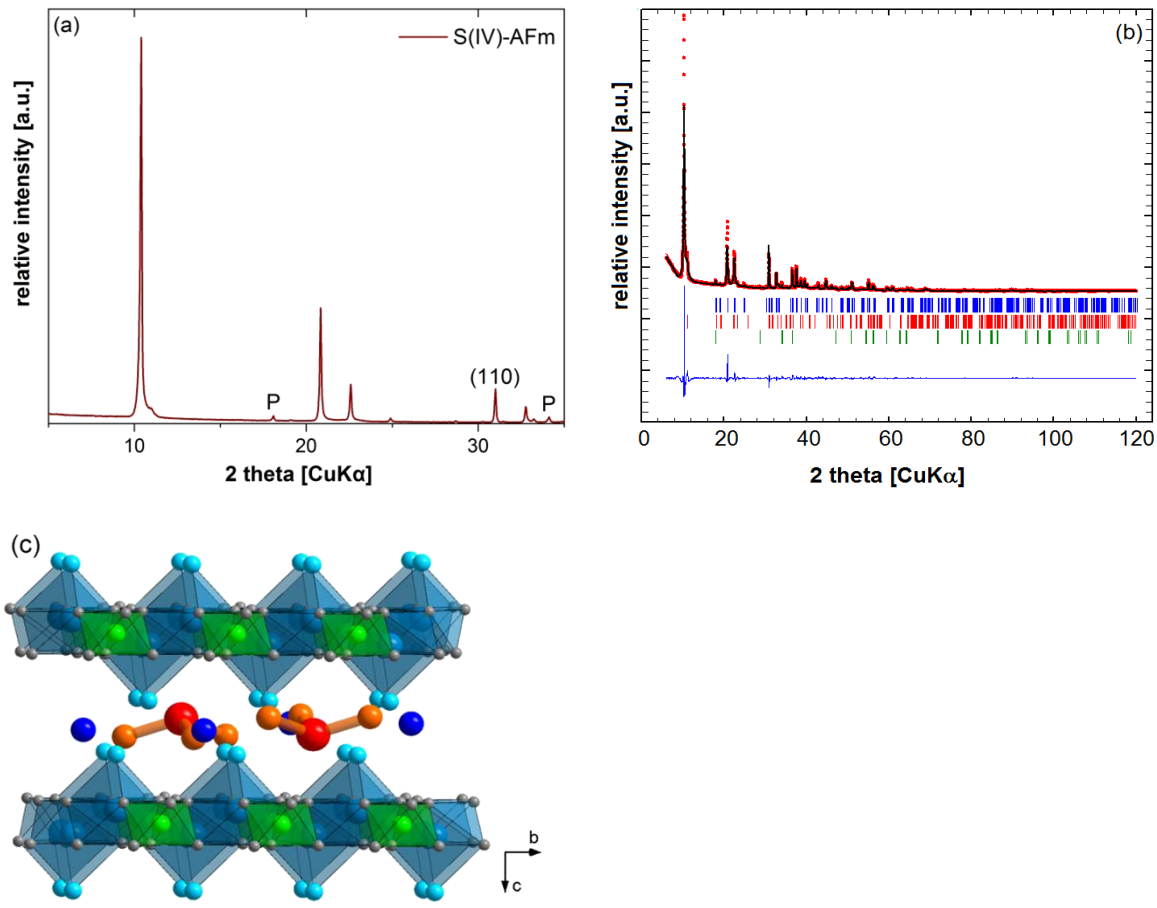

Figure 3: (a) XRPD pattern and (b) Rietveld plot of the S(IV)-AFm sample (pH~13) showing the diffraction experimental pattern (red dots), the calculated pattern (black line), the difference curve (blue line) and sticks for Bragg peaks positions for the resolved S(IV)-AFm phase (blue), for the unresolved underhydrate $3CaO{\cdot}Al_2O_3{\cdot}CaSO_3{\cdot}XH_2O$ (red) and for portlandite impurity (green). P: portlandite. (c) General representation of the structural model for the S(IV)-AFm phase, projection almost along [100]. The SO_3^{2-} anion is shown in red and orange, the Ca polyhedra in light blue, Al octahedra in green, hydroxyl in grey, bonded water from the main layer in light blue and interlayer water molecules in dark blue. For clarity reasons, the disordered interlayer part of the structure is presented in an ordered way.

305 **Table 1:** Rietveld refinement of the S(IV)-AFm phase. Standard deviations (σ values from Rietveld
306 treatments) are indicated in parentheses.

Atom	Site	*x*	*y*	*z*	B_{iso}	Occupancy
$R\bar{3}$, Z=3						
a = 5.7693(6) Å, *c* = 25.533(1) Å, V = 736.0(1) Å^3						
R_{Bragg} = 0.034, R_p = 0.14, R_{wp} = 0.16						
Al	3*a*	0	0	0	1.0(-)	1(-)
Ca	6*c*	2/3	1/3	0.0220(3)	1.0(-)	1(-)
O1 (OH^-)	18*f*	0.253(3)	0.940(3)	0.0370(9)	1.0(-)	1(-)
O2 (H_2O)	6*c*	0	0	0.7875(9)	1.0(-)	1(-)
S	6*c*	0	0	0.489(1)	1.0(-)	¼(-)
O3 (SO_3)	18*f*	0.08(1)	0.269(6)	0.513(2)	1.0(-)	¼(-)
O4 (H_2O)	3*b*	0	0	0.5	1.0(-)	0.06(2)

307

308

309 3.1.3 Se(IV)-AFm: From all synthesized samples, the Se(IV)-AFm was found to be the least crys-
310 talline AFm phase. The crystallinity of the phase showed no clear dependence on the aging time, how-
311 ever, a pH dependence was observed: a Se(IV)-AFm formed at pH~13 has only weakly defined diffrac-
312 tion peaks, whereas at pH~12 the diffraction peaks are more intense (Fig. 4). Therefore, the crystal
313 structure analysis was only carried out for the AFm sample synthesized at pH~12. The structure analy-
314 sis was still limited due to the presence of two distinct AFm phases – i.e. two Se(IV)-AFm hydrates.
315 These two hydrates seem to have a hexagonal unit cell with the refined interlayer distances 11.05 Å
316 and 9.65 Å, respectively.

317 Ma et al. [41] observed the formation of Se(IV)-AFm phases with two distinct interlayer distances in a
318 series of sorption experiments of SeO_3^{2-} onto Cl-AFm and SO_4-AFm. SeO_3^{2-} intercalation in the inter-

layer resulted in the formation of Se(IV)-AFm phases with interlayer distances 11.01±0.01 Å and 9.99±0.01 Å in the case of the Cl-AFm, and 11.06±0.01 Å and 9.87±0.01 Å in the case of the SO_4-AFm. Based on EXAFS experiments, the authors attributed the two types of Se(IV)-AFm formed to different complexation configurations of the SeO_3^{2-} anions in the interlayer: the phases with the larger spacing of ~11.1 Å contain free hydrated SeO_3^{2-}, whereas inner-sphere complexation of Se accounts for the smaller d-values of ~9.9 Å. The two Se(IV)-AFm hydrates observed in this study show similar interlayer distances to the ones investigated earlier by Ma et al. [41] suggesting that the differences may arise from the different types of coordination environments of the intercalated SeO_3^{2-} anions. While the 9.65 Å hydrate might contain SeO_3^{2-} bonded to the main layer, the larger d-value of the 11.05 Å hydrate could be explained with free Se(IV) in the interlayer.

The Se(IV)-AFm structural analysis has shown two distinct symmetries for the two hydrates: a rhombohedral symmetry with a hexagonal axis corresponding to three interlayers for the 11.05 Å hydrate ($R\bar{3}$, Z=3, a = 5.7752(9) Å, c = 33.162(12) Å) and a trigonal symmetry with a hexagonal axis corresponding to two interlayers for the 9.65 Å hydrate ($P\bar{3}$, Z=2, a = 5.7752(9) Å, c = 19.300(9)Å). A structure solution has been searched for the 9.65 Å hydrate with the FOX software using two independent main layers, two independent water molecules and one selenite group. The SeO_3 geometry has been fixed with Se-O distances of 1.69 Å, O-O distances of 2.64 Å and O-Se-O angle of 103° according to distances and angles averages from the $CaSeO_3$ crystal structure [42]. Structural models proposed by FOX [34] invariably suggest selenite anion in front of calcium cations from one main layer out of two, explaining thus the periodicity based on two interlayers. Selenite anions are oriented almost perpendicularly to the layers with the four atoms (one selenium atom and three independent oxygen atoms) located on general positions with half of one third occupancies (to respect electro-neutrality). The best solution found is presented in Table 2. All the proposed structural models could not be refined with FullProf [35], most probably due to a non-hexagonal real symmetry (monoclinic or triclinic lowering of symmetry). The proposed structure for the Se(IV)-AFm is very similar to the one of the NO_3-AFm [10], in which the anion is bonded to a calcium, is oriented perpendicularly to the main layer and shows disor-

der around the trigonal (or pseudo-trigonal) axis. The selenite anion is connected to a calcium cation via a bidentate ionic bonding with two Ca2-O5 and Ca2-O6 distances of about 2.5 Å, similarly to the calcium environment in the $CaSeO_3$ crystal structure [42]. It is interesting to note that this structural organization corresponds to the one found by Ma et al. [41] for their 9.87 Å Se(IV)-AFm based on EXAFS measurements. The lack of better quality powder patterns (despite numerous attempts to synthesize a single phase sample with high crystallinity), or more simply the absence of single crystals, did not allow further structural resolution of the 9.65 Å Se(IV)-AFm compound, nor was it possible to work on a structural model for the 11.05 Å Se(IV)-AFm compound.

Table 2: Best – unrefined – structure solution proposed by FOX software for the Se(IV)-AFm phase of composition $[Ca_2Al(OH)_6]\cdot½SeO_3\cdot3H_2O$.

Atom	Site	*x*	*y*	*z*	Occupancy
$P\bar{3}$, Z=2					
a = 5.7752(9) Å, *c* = 19.300(9) Å, V = 560.0(6) Å^3					
Al1	1*a*	0	0	0	1
Al2	1*b*	0	0	1/2	1
Ca1	2*d*	2/3	1/3	-0.030	1
Ca2	2*d*	2/3	1/3	0.470	1
O1 (OH^-)	6*g*	0.00	-0.28	-0.055	1
O2 (OH^-)	6*g*	0.27	0.27	0.558	1
O3 (H_2O)	2*d*	2/3	1/3	-0.160	1
O4 (H_2O)	2*d*	2/3	1/3	0.340	1/2
Se	6*g*	0.93	0.38	0.32	1/6
O5 (SeO_3)	6*g*	0.00	0.65	0.37	1/6
O6 (SeO_3)	6*g*	0.62	0.14	0.35	1/6
O7 (SeO_3)	6*g*	0.86	0.47	0.24	1/6
O5 (H_2O)	2*c*	0	0	0.25	1/2

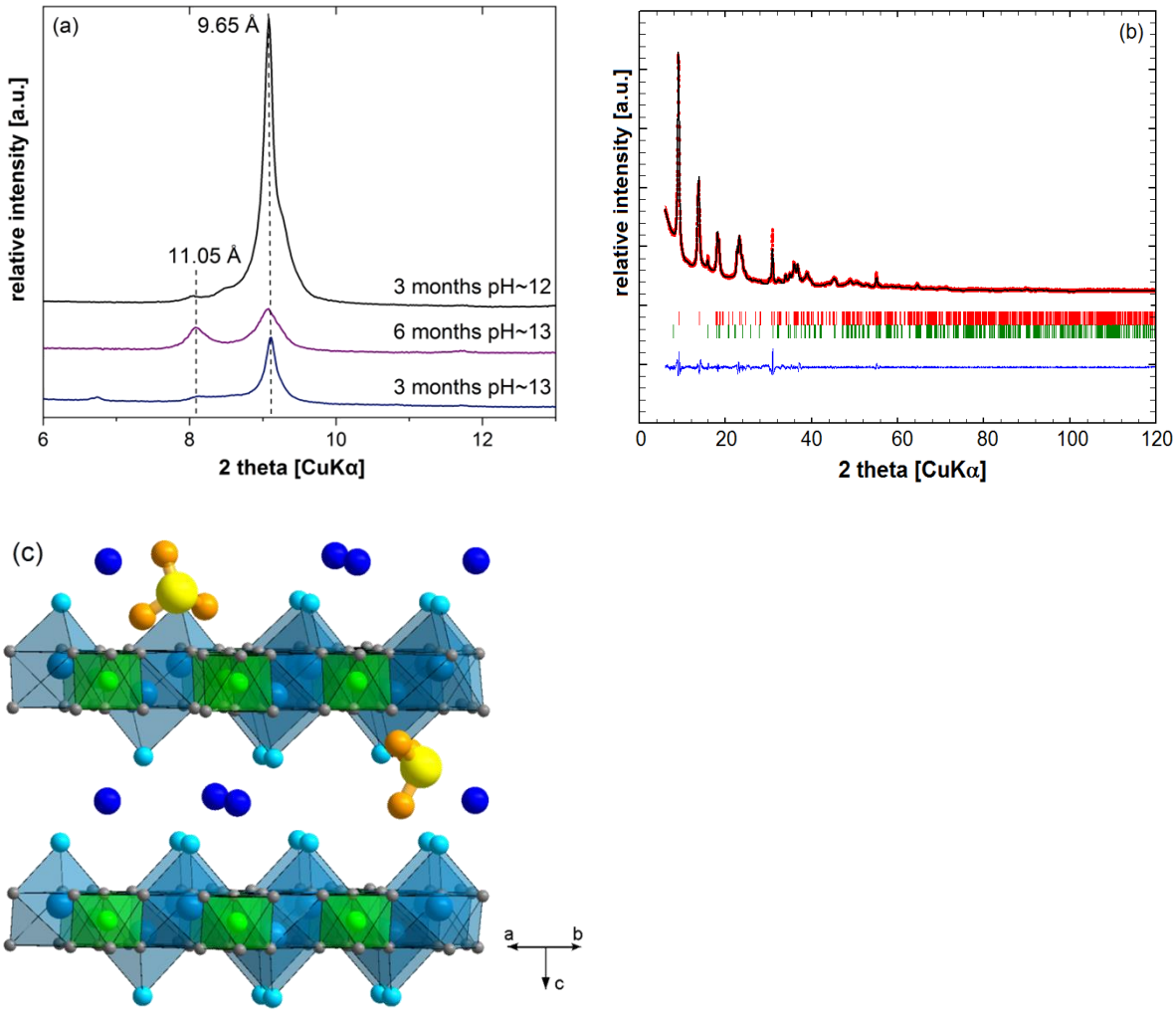

Figure 4: (a) XRPD pattern of the Se(IV)-AFm phase synthesized at different pH. The samples were dried over a saturated NaOH-solution (RH ~8 %). (b) Rietveld plot of the Se(IV)-AFm sample (pH~12) showing the diffraction experimental pattern (red dots), the calculated pattern (black line), the difference curve (blue line) and sticks for Bragg peaks position for the two Se(IV)-AFm hydrates with the interlayer distance 9.65 Å (red) and 11.05 Å (green). (c) General representation of the suggested structural model for the 9.65 Å hydrate, projection almost along [110]. The SeO_3^{2-} anion is shown in yellow and orange, the Ca polyhedra in light blue, Al octahedra in green, hydroxyl in grey, bonded water from the main layer in light blue and interlayer water molecules in dark blue. For clarity reasons, the disordered interlayer part of the structure is presented in an ordered way.

3.1.4 Se(VI)-AFm: The XRPD pattern of the Se(VI)-AFm sample shows a well crystallized phase with numerous diffraction peaks corresponding to a symmetry lower than rhombohedral or trigonal. The diffraction pattern correlates to an apparent monoclinic lattice with the following refined parameters: a = 10.5741(4) Å, b = 4.9846(2) Å, c = 8.6316(3) Å and β = 105.759(4)°, and an interlayer distance of 10.18 Å. However, the monoclinic unit cell volume of 438 $Å^3$ for the interlayer distance of 10.18 Å corresponds to a composition 1.5 $[Ca_2Al(OH)_6]\cdot½SeO_4\cdot nH_2O$ which is inconsistent with crystallographic considerations. Attempts to solve the structure using a lower-symmetry triclinic unit cell were inconclusive and no other set of lattice parameters could be found with X-Cell [33]. At this stage single crystal data are needed to pursue crystallographic investigations. The Se(VI)-AFm lattice seems to be unrelated to previously known low-symmetry structures found in the AFm family such as the monoclinic Friedel's salt (Cl-AFm) [43] or the triclinic monocarbonate (CO_3-AFm) [44].

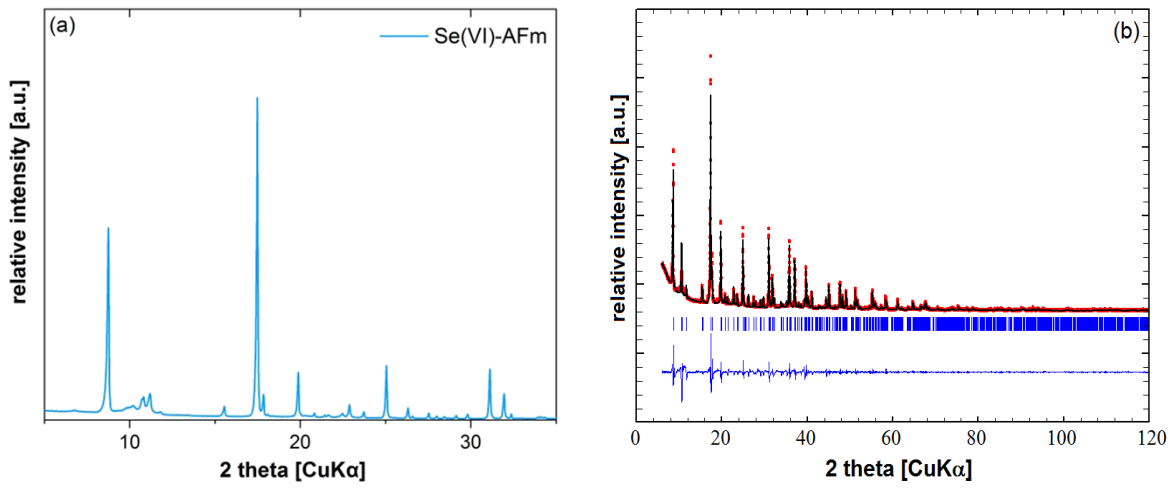

Figure 5: (a) XRPD pattern and (b) Rietveld plot of the Se(VI)-AFm sample using the monoclinic lattice parameters.

3.1.5 S(II)-AFm: The powder pattern of the S(II)-AFm sample resembles a rhombohedral AFm structure with an interlayer distance of 10.33 Å. However, a diffraction peak cluster at ~11° was observed which cannot be explained by a rhombohedral symmetry. The use of a monoclinic unit cell with the lattice parameters a = 10.469(1) Å, b = 5.7736(7) Å, c = 9.982(1) Å and β = 98.964(8)° partially explains this diffraction peak cluster (Fig. 6). This monoclinic unit cell is related to the monoclinic structure of Friedel's salt.

Since this monoclinic lattice explains only partially the diffraction peaks, and since no structural model could be found in the monoclinic symmetry, structure solution using FOX has been performed into the average rhombohedral lattice. $S_2O_3^{2-}$ geometry has been fixed to S-S bond distance of 2.10 Å, S-O bond distance of 1.55 Å, S-S-O angles of 103° and O-S-O angles of 107°. Invariably, obtained structure solutions indicate a perpendicular orientation of the $S_2O_3^{2-}$ anion with the end-sulfur atom directed toward calcium cation. Although the structure solution models suggest an inclination of the S-S bond toward the trigonal axis, structure parameters gathered in Table 3 correspond to an average configuration with a more symmetrical situation: $S_2O_3^{2-}$ oriented along the trigonal axis with both sulfur atom in a special 6*c* Wyckoff site; i.e. with a perfectly normal orientation to the main layer.

Table 3: Average – unrefined – structure solution proposed by FOX for the S(II)-AFm phase of composition $[Ca_2Al(OH)_6]\cdot\frac{1}{2}S_2O_3\cdot 3H_2O$.

Atom	Site	*x*	*y*	*z*	Occupancy
$R\bar{3}$, Z=3					
a = 5.7660(6) Å, *c* = 30.9821(6) Å, V = 892.1(4) Å^3					
Al	3*a*	0	0	0	1
Ca	6*c*	2/3	1/3	0.016	1
O1 (OH^-)	18*f*	0.2916	0.2493	0.035	1
O2 (H_2O)	6*c*	2/3	1/3	0.100	3/4
O3 (H_2O)	6*c*	1/3	2/3	0.167	3/4
S1	6*c*	2/3	1/3	0.100	1/4
S2	6*c*	2/3	1/3	0.167	1/4
O4 (S_2O_3)	18*f*	0.902	0.306	0.186	1/4

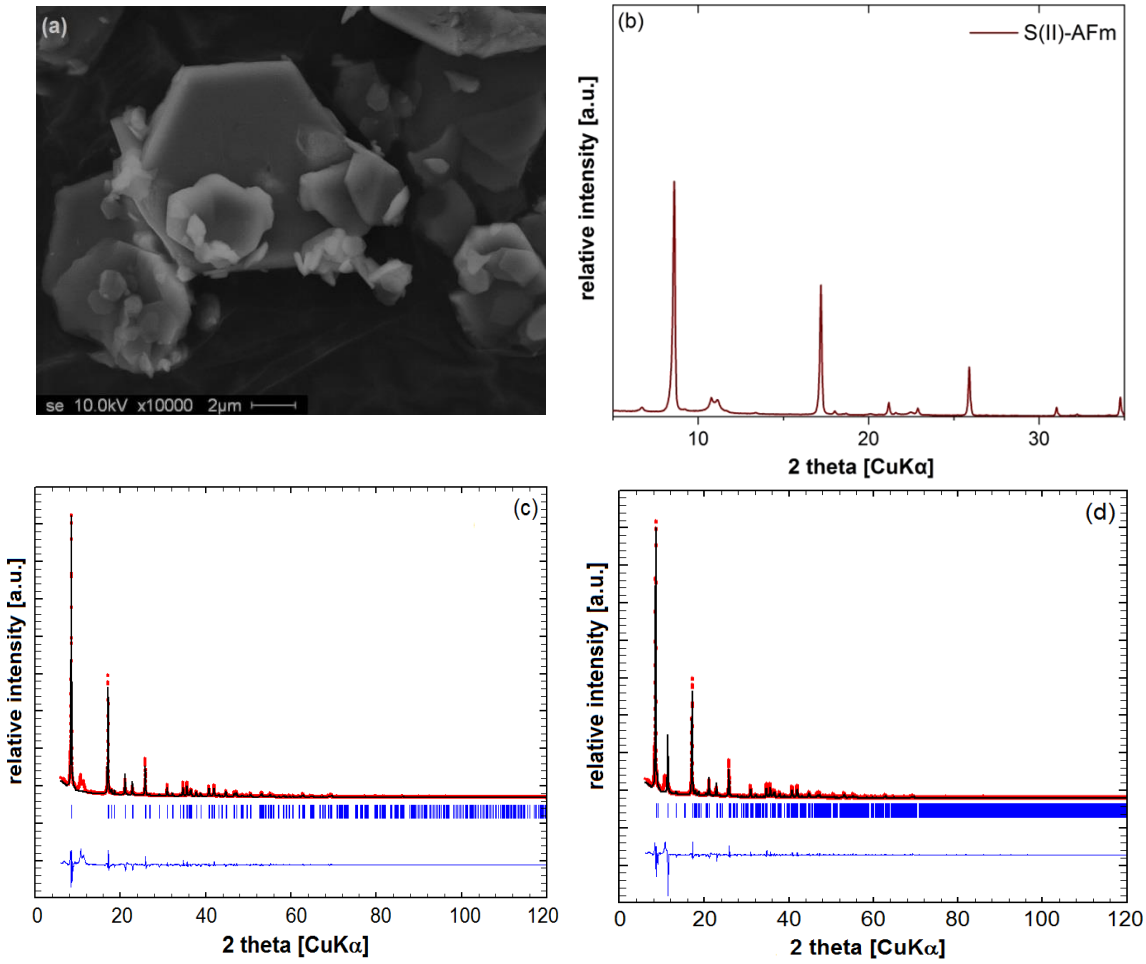

Figure 6: (a) SEM image of the S(II)-AFm showing the typical lamellar shape; XRPD pattern (b) and Rietveld plot of the S(II)-AFm sample using a hexagonal (c) and a monoclinic (d) unit cell.

Based on the best structural model found for each AFm phase, the densities of the phases were also calculated. The values are compiled in Table 4 together with further crystallographic data.

455 **Table 4:** Summary of crystallographic data for the S- and Se-containing AFm phases.

AFm Phase	Empirical Formula	System	Z	Cell Volume [Å^3]	Interlayer Distance [Å^3]	Density [g/cm^3]
S(VI)[25]	$AlCa_2H_{12}O_{11}S_{0.5}$	rhombohedral	3	769.50	8.93	2.02
S(IV)	$AlCa_2H_{10.2}O_{9.6}S_{0.5}$	rhombohedral	3	736.0(1)*	8.51*	1.94*
Se(IV)	$AlCa_2H_{12}O_{10}Se_{0.5}$	trigonal	2	560.0(6)*	9.65*	1.94*
Se(VI)	$AlCa_2H_{12}O_{11}Se_{0.5}$	monoclinic*	1.5	(438)*	10.18*	1.90*
S(II)	$AlCa_2H_{12}O_{10.5}S$	rhombohedral*	3	892.1(4)*	10.33*	1.78*

456 * tentative values based on the best structural model found from the XRPD data.

457

458

459 3.2. Water in the AFm phases:

460 The binding of water in the synthesized AFm phases was investigated by several techniques.

461 3.2.1 TGA: The hydration state of the samples was determined by measuring the weight loss in
462 the temperature region between 30°C and 600°C. Weight losses above this temperature are associated
463 with sulfur decomposition and loss of CO_2 (at ~700°C), which is present in minor amounts due to at-
464 mospheric contamination (<1.5 wt.%). Therefore, weight loss above 600°C was not taken into consid-
465 eration.

466 The TGA-DTG curves (Fig. 7) of all synthesized samples show stepwise water removal, which was ob-
467 served in the temperature regions characteristic for AFm phases [45]. Loosely bound water from the in-
468 terlayer is lost in three temperature steps which vary in size and range for the different samples. In
469 general, however, water removal from the interlayer occurs up to a temperature of ~250°C. In the
470 temperature region between 250°C and 600°C the six main layer waters of $Ca_4Al_2(OH)_{12}^{2+}$ are lost. A
471 weight loss at ~450°C indicates the presence of portlandite impurities as found in the S(IV)-AFm. The

total mass losses add up to ~30 wt.% for S(IV)-AFm, ~32 wt.% for Se(IV)-AFm, ~33 wt.% for S(II)- and Se(VI)-AFm, and ~35 wt.% for S(VI)-AFm. The number of H_2O molecules was calculated as ~11 H_2O for S(IV)- and Se(IV)-AFm, ~12 H_2O for S(VI)-AFm, and ~13 H_2O for S(II)- and Se(VI)-AFm, respectively.

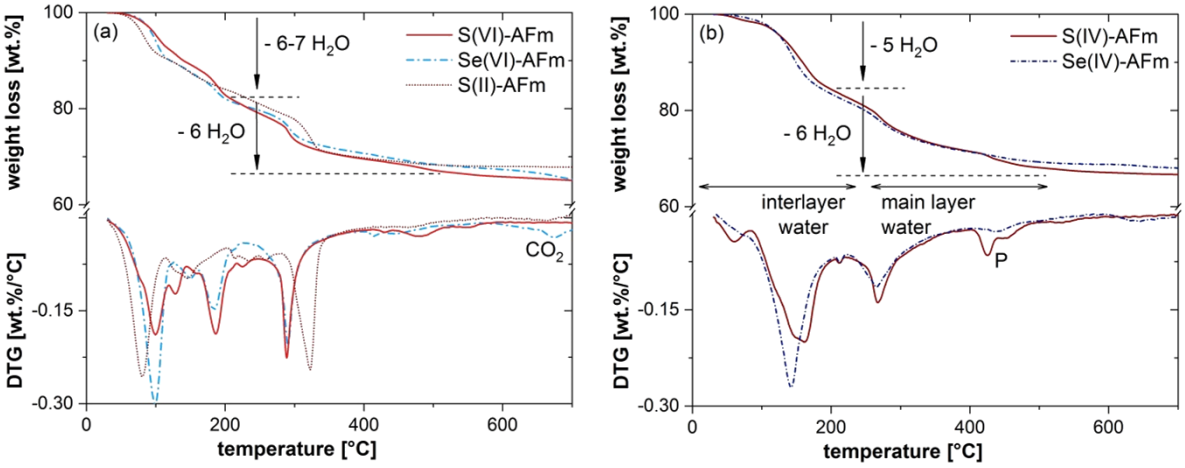

Figure 7: TGA data for the studied AFm phases synthesized at pH~13. The samples were dried over a saturated NaOH solution (RH ~8 %). P: portlandite.

3.2.2 FTIR/Raman spectra: Figure 8 shows the FTIR spectra recorded between 600 and 4000 cm^{-1} and the Raman spectra recorded between 55 and 3700 cm^{-1} of the samples.

To better understand the FTIR and Raman spectra of the interlayer anions, the observed peak positions are compared with literature data for the free anions in solution [46-48] to detect possible changes in the spectral behaviour caused by the structural environment in the AFm phase (Table 5). The assignment of the peak positions of the anions was also verified by comparison with FTIR measurements on the Na_2-sulfur salts used for the synthesis. In carbonate (CO_3^{2-}) containing AFm phases, for instance, two band positions for the Raman-active symmetric stretching mode (ν_1) can be found: an absorption band at ~1086 cm^{-1} is characteristic for a weakly bonded CO_3^{2-} in the centre of the interlayer; while in

the cases where the carbonate is bonded to the main layer (via a Ca) a shift towards lower wave-numbers is observed and the $v_1(CO_3^{2-})$ vibration occurs at ~1068 cm^{-1} [16].

The free SO_4^{2-} and SeO_4^{2-} anions have a T_d symmetry with the symmetric stretching mode v_1 and bending mode v_2 Raman active only and the asymmetric stretching mode v_3 and bending mode v_4 both FTIR and Raman active [46]. In monosulfate, due to the interactions with the crystal structure, the point symmetry of SO_4^{2-} is lowered, leading to the splitting of the v_1 and v_3 modes into two components: v_1, v_1`, $v_3$ and $v_3$`, respectively [49]. In the FTIR spectrum of the S(VI)-AFm (Figure 8a), the v_3 is visible as a strong, broad absorption peak at ~1100 cm^{-1} with a shoulder at ~1160 cm^{-1} (v_3`). A very weak absorption band at ~620 $cm^{-1}$ is also observed, which could be attributed to the $v_4$ mode. The Raman spectrum of the phase shows the $v_1$ at ~982 $cm^{-1}$; with a shoulder at ~990 $cm^{-1}$ belonging to the $v_1$` component. The v_2 and v_4 modes are present at ~450 and ~615 cm^{-1}, respectively; at positions similar to the ones of the free SO_4^{2-} anion. The v_3 absorption band cannot be clearly distinguished; however, a broad, low intensity band is observed between 1090 and 1160 cm^{-1}, suggesting splitting of the v_3 band. The $v_3(SeO_4^{2-})$ mode in the Se(VI)-AFm is visible at ~874 cm^{-1} by FTIR and ~870 cm^{-1} by Raman, where it overlaps with the symmetric stretching v_1 mode (~835 cm^{-1}). The two signals at ~335 and ~395 cm^{-1} are most probably caused by the bending v_2 and v_4 modes, occurring thus at slightly lower wavenumbers than expected for the free SeO_4^{2-} (v_2: ~345 cm^{-1} and v_4: ~412 cm^{-1} [47]).

Free SO_3^{2-} and SeO_3^{2-} anions have C_{3v} point symmetry with the four normal modes both FTIR and Raman active [46]. In the S(IV)-AFm, the $v_3(SO_3^{2-})$ mode is seen in FTIR as a very broad, asymmetric absorption band at ~955 cm^{-1}, possibly caused by overlapping with the v_1 band (at ~967 cm^{-1} for the free SO_3^{2-} [48]) and/or by splitting. The FTIR spectrum of the phase is further characterized by another broad band, consisting of at least two overlapping components at ~695 and 745 cm^{-1} (Figure 8c). In Raman the bending v_2 and v_4 modes occur as weak signals at ~620 and ~480 cm^{-1}; while the overlapping bands at ~975 and ~995 cm^{-1} are most probably due to the v_1 and v_3 modes. The v_3 mode in the Se(IV)-AFm is observed in FTIR at ~730 cm^{-1} with a shoulder at ~800 cm^{-1} corresponding to the v_1 mode. In Raman, the two modes are observed in the same positions with additional shoulder at ~780

cm^{-1} indicating splitting of the v_1 band. The v_4 mode is visible at ~374 cm^{-1}; the v_2 at ~455 cm^{-1}, which implies a slight shift of the v_2 mode to higher wavenumbers.

The free $S_2O_3^{2-}$ anion has a C_{3v} point symmetry with six FTIR and Raman active vibrational modes [46]. All six bands can be identified in the Raman spectrum of the S(II)-AFm, appearing at positions close to the ones expected for the free $S_2O_3^{2-}$ anion with exception of the v_2 mode, which seems to be shifted towards lower wavenumbers at ~630 cm^{-1} compared to 669 cm^{-1} for $S_2O_3^{2-}$ measured in solution [47]. In FTIR, however, the v_2 band is observed without a shift at ~670 cm^{-1}, together with the v_1 (~1010 cm^{-1}) and v_4 (~1130 cm^{-1}) modes as well as a shoulder at ~1070 cm^{-1} (Figure 8e).

Two types of hydrous components can be distinguished in the FTIR spectra of the samples. Interlayer H_2O is visible by absorption bands in the 3600 – 3000 cm^{-1} and in the 1650 – 1600 cm^{-1} region. Less resolved spectra between 3600 and 3000 cm^{-1} indicate disorder in the interlayer [49]. Such is the case with the S(VI)-, the Se(VI)- and the S(II)-AFm phases. In contrast, better ordered interlayer water is indicated in case of the S(IV)- and the Se(IV)-AFm. The water from the main layer, on the other hand, is visible by absorption at ~3670 – 3650 cm^{-1}, which is attributed to the hydroxyl symmetric stretching mode. In the Raman spectra similar patterns can be observed. The broad signal at ~2800 – 3600 cm^{-1} is attributed to water bonded in the interlayer, whereas the sharp peak at ~3688 cm^{-1} is caused by the OH groups from the main layer [49]. The band position for $Al(OH)_6$ appears at ~532 cm^{-1} for all investigated samples as also observed for other AFm phases [16, 49]. The small absorption bands at 1450 – 1250 cm^{-1} in the FTIR and at ~1086 cm^{-1} in the Raman spectra corresponds to weakly bound carbonate in the interlayer indicating minor CO_2 contamination.

Table 5: Summary of the main vibrational frequencies observed in the FTIR and Raman spectra of the synthesized AFm phases; as well as comparison with literature data for the free SO_4^{2-}, SeO_4^{2-}, SO_3^{2-}, SeO_3^{2-} and $S_2O_3^{2-}$ anions.

Species	ν_1 [cm^{-1}]	ν_2 [cm^{-1}]	ν_3 [cm^{-1}]	ν_4 [cm^{-1}]	ν_5 [cm^{-1}]	ν_6 [cm^{-1}]	Method
$SO_4^{2-}{}_{(aq)}$[46]	983	450	1105	611			FTIR/Raman
S(VI)-AFm[t.s.]	-	n.d.	1100/1160	620			FTIR
S(VI)-AFm[49], t.s.	982/990	450	1090/1160	615			Raman
$SeO_4^{2-}{}_{(aq)}$[47]	832	345	879	412			FTIR/Raman
Se(VI)-AFm[t.s.]		n.d.	874	n.d.			FTIR
Se(VI)-AFm[t.s.]	835	335?	870	395?			Raman
$S_2O_3^{2-}{}_{(aq)}$[47]	995	669	446	1123	541	335	FTIR/Raman
S(II)-AFm[t.s.]	1010	670	n.d.	1130	n.d.	n.d.	FTIR
S(II)-AFm[t.s.]	995	630	442	1125	541	327	Raman
$SO_3^{2-}{}_{(aq)}$[48]	967	620	933	469			FTIR/Raman
S(IV)-AFm[t.s.]	-	-	955	n.d.			FTIR
S(IV)-AFm[t.s.]	995?	620	975?	480			Raman
$SeO_3^{2-}{}_{(aq)}$[47]	807	432	737	374			FTIR/Raman
Se(IV)-AFm[t.s.]	800	n.d.	730	n.d.			FTIR
Se(IV)-AFm[t.s.]	780/800	455	730	374			Raman
$Al(OH)_6$[16, 49], t.s.		532					Raman
H_2O interlayer[49], t.s.	3000-3600	1600-1650					FTIR/Raman
OH main layer[49], t.s.	3650-3670						FTIR/Raman
CO_3^{2-}[16], t.s.	1086		1250-1450				FTIR/Raman

n.d.: no data; t.s.: this study

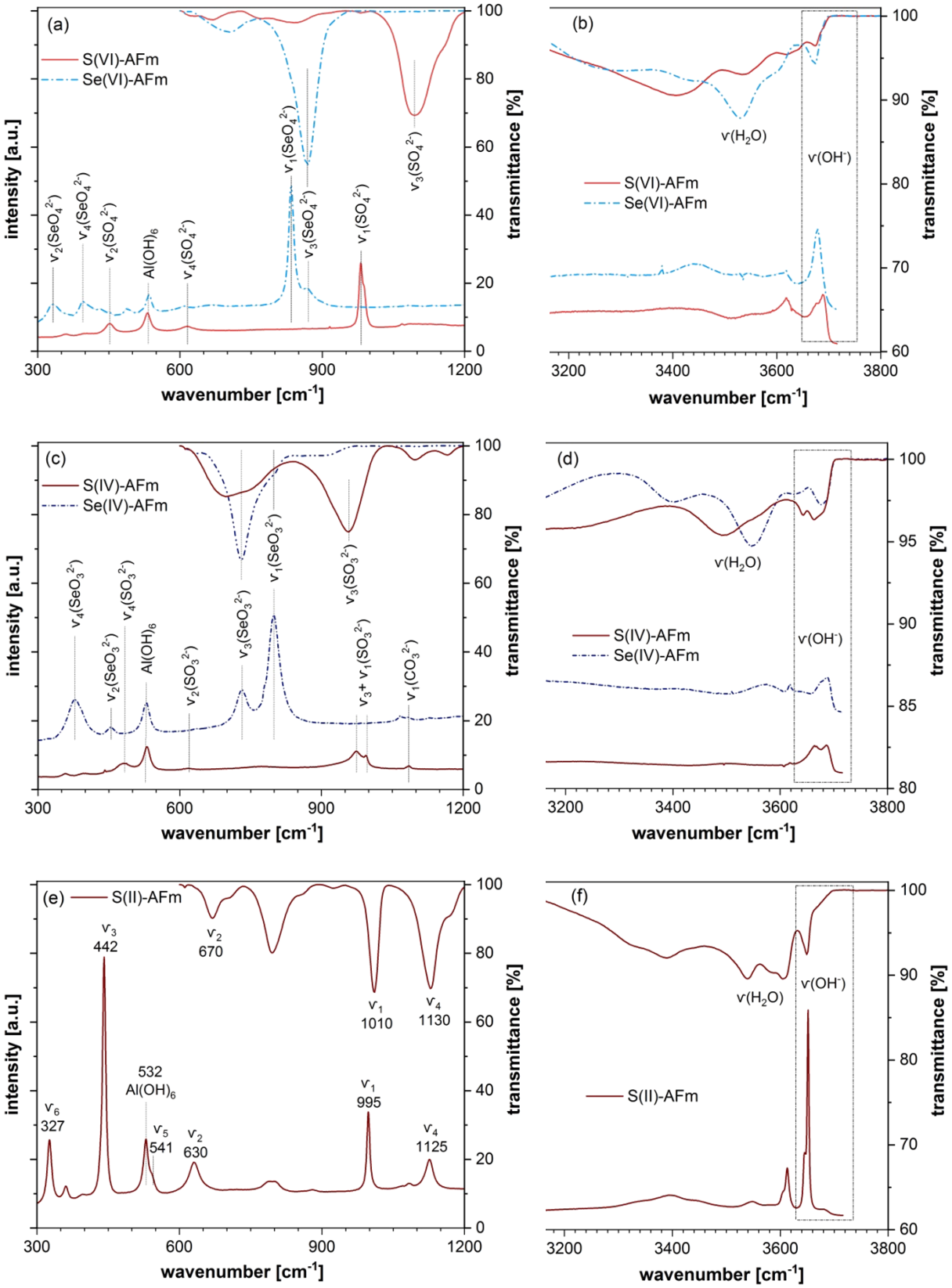

Figure 8: FTIR (top) and Raman (bottom) spectra of the synthesized AFm phases in the frequencies ranges of the interlayer anions (300 – 1200 cm^{-1}) and the hydrogen bond network (3200 – 3800 cm^{-1}).

The FTIR and Raman spectra confirm the presence of AFm phases with their typical $Al(OH)_6$-vibration in the ~530 cm^{-1} region (Raman shift) and further allow the different interlayer ions to be identified. No clear conclusions can be made regarding the orientation of the interlayer anions to either confirm or disregard the proposed structural arrangements for the studied AFm phases.

3.2.3 DVS: Based on the initial composition obtained by TGA, the change of the hydration level of the samples as a function of the relative humidity was examined. The sorption experiments were carried out on samples which had been stored for 1 year in a desiccator over a saturated NaOH solution (RH ~8 %). The data were normalized to the water content determined by TGA at 8 % RH for each sample.

The DVS of the S(VI)-AFm has been detailed in Baquerizo et al. [26]. The S(VI)-AFm contains 10.5 H_2O per formula unit below ~30 % RH, 12 H_2O between 30 and 97 % RH and 14 H_2O above 97 % RH. The S(II)-AFm shows only a single absorption step at low RH and no further changes (Fig. 9). At 5 % RH a 9 H_2O hydrate is observed, which transforms to a 13 H_2O hydrate at 30 % RH and dehydrates back to 9 H_2O between 10 and 20 % RH in the desorption cycle. For the Se(IV)-AFm a stable hydration state of 11 H_2O was observed which shows no changes with increasing RH. The minimal total water content achieved for the Se(VI)-AFm is 12 H_2O at 5 % RH. The hydration state of the sample increases to 13 H_2O at 10 % RH and remains stable up to 95 % RH. Desorption occurs at 10 % RH. For the S(IV)-AFm phase an initial hydration state of 11 H_2O is observed, which remains stable up to 70 % RH (Fig. 10). Between 70 and 95 % RH the sample undergoes a steady water uptake reaching 40 H_2O at 95 % RH and dehydrates back to 11 H_2O at 70 % RH. Due to the unusually high hydration level observed, a second measurement was performed on the S(IV)-AFm sample to verify the acquired data, giving almost identical results.

The sorption isotherms for the S(II)-AFm, Se(IV)-AFm and Se(VI)-AFm phases show a similar evolution with a water decrease at lower RH (5 – 30 % RH), followed by a plateau at higher RH. This general trend had also been observed for other AFm phases (S(VI)-AFm [26], monocarbonate, hemicarbonate and hydroxy-AFm [27]). The high water uptake of the S(IV)-AFm at high RH could possibly be the result of water condensation on the surface.

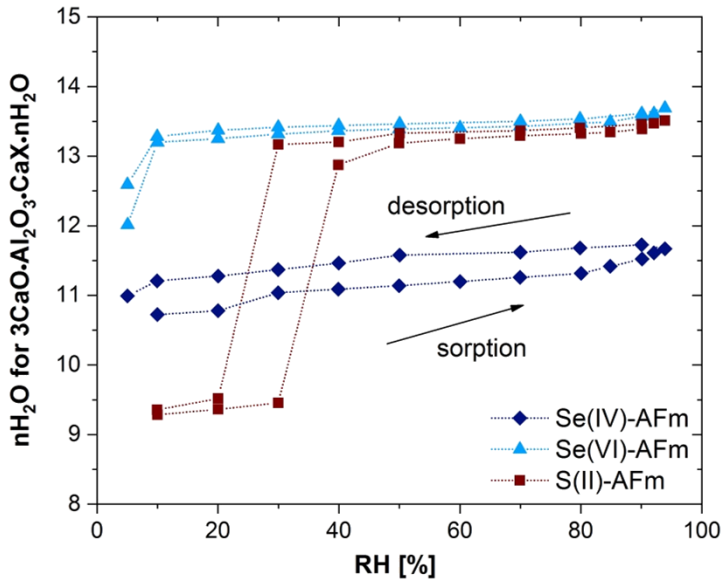

Figure 9: Sorption isotherms for the S(II)-, Se(IV)- and Se(VI)-AFm phases measured at 25°C. The graph was normalized to the n H_2O determined by TGA at 8 % RH for each sample.

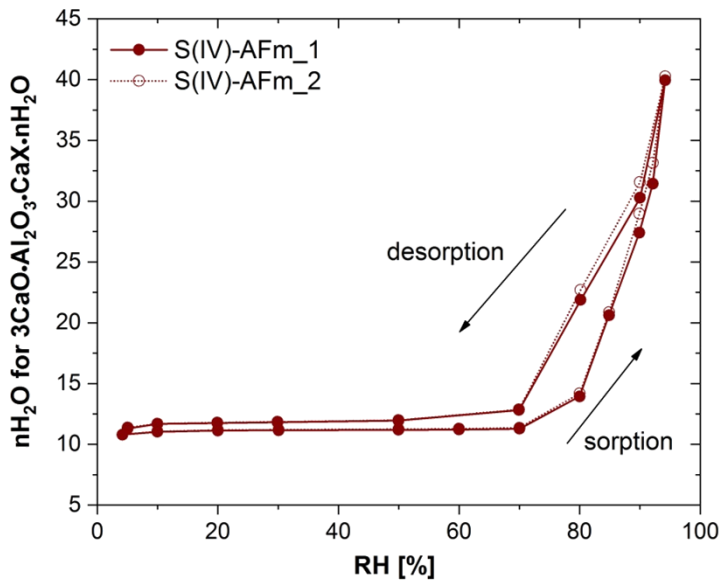

Figure 10: Sorption isotherms for the S(IV)-AFm phase measured at 25°C showing the two measurements S(IV)-AFm_1 and S(IV)-AFm_2. The graph was normalized to the 11 H_2O determined by TGA at 8 % RH.

3.3 Solubility products: From the measured aqueous concentrations (data compiled in Appendix A.1 and A.2) the solubility products for the different AFm phases were calculated. The solubility products are plotted in Figure 11 for different aging times (3 vs. 6 months) and different pH values (pH~13 vs. pH~12 for the S(VI)- and the Se(IV)-AFm). For the calculations the highest hydration state of each phase as observed in the DVS measurements was used; solely for the S(IV)-AFm the high hydration state of 40 H_2O, which is most probably due to water condensation on the surface, was neglected and the solubility product calculated with 11 H_2O. The calculated solubility products (log K) for all AFm phases are similar with mean values ranging between -30.5±1.1 (S(II)-AFm) and -26.9±1.1 (S(IV)-AFm) (Table 6). The S(IV)-AFm shows the least negative value suggesting thus that it is the least stable phase. The largest scatter in calculated solubility products was observed for the S(VI)-AFm with values between -27.5 to -30.2 and for the Se(IV)-AFm (-25.5 to -30.9). The solubility of the S(VI)-AFm seems to decrease at high pH. At pH~13 the solubility products are less negative which could be due

to the formation of a solid solution between hydroxyl-AFm (OH-AFm) and S(VI)-AFm as discussed in detail by Matschei et al. [3]. A portion of the SO_4^{2-} in the interlayer is substituted by OH^- leading to the formation of an (S(VI)-OH)-AFm phase with an apparent higher solubility product, compared to pure S(VI)-AFm (mean value for all measurements at pH~13 log K = -28.1±0.7 compared to the solubility products obtained at pH~12 log K = -30.2±0.7). The latter value is also closer to the values of -29.3 to -29.8 reported in recent literature [14, 19, 50], where the solubility was also determined at pH~12. The solubility products determined for the Se(IV)-AFm are very similar with -28.2±1.6 at pH~13 and -28.5±0.7 at pH~12. However, at the higher pH, the scatter is relatively large which could be related to the lower degree of crystallinity of the samples at higher pH values as shown in Figure 4. However, the solubility product of Se(IV)-AFm with -28.4±0.8 agrees well with the solubility of -28.1 recently determined by Ma et al. [41]. The Se(VI)-AFm has a solubility product of -29.2±1.5 showing the least scatter and agrees well with the value of -28.6 published earlier by Baur & Johnson [51] within the error. The aging time seems to have no pronounced effect on the samples stability as the calculated solubility products after 6 months are comparable to those after 3 months within the errors.

The solubility products for S(VI)-, S(IV)-, S(II)-, Se(VI)- and Se(IV)-AFm phases are all similar with mean values of -26.9 to -30.5. These solubility products are also comparable to the solubility of other AFm phases containing oxyanions, such as the -28.4 reported for CrO_4-AFm [14] or -27.8 for MoO_4-AFm [15]. These similar solubilities of the AFm phases with oxyanions suggest that the sulfur concentration in the pore solution of the cement will strongly affect Se binding by AFm phases; high sulfur concentration are expected to lower Se binding.

Table 6: Mean solubility products (log K), Gibbs energy of formation ($\Delta_f G^0$), enthalpy of formation ($\Delta_f H^0$), entropy (S^0), heat capacity (C_p^0) and molar volume (V^0) calculated for the synthesized AFm phases at 20°C and 1 bar.

Phase	Log K	$\Delta_f G^0$ [kJ/mol]	$\Delta_f H^0$ [kJ/mol]	S^0 [J/mol·K]	C_p^0 [J/mol·K]	V^0 [cm^3/mol]
S(VI)-AFm $3CaO \cdot Al_2O_3 \cdot CaSO_4 \cdot 14H_2O$	-28.8 ±1.2	-8009	-9031	891.0	1017.8	331[26]
S(IV)-AFm $3CaO \cdot Al_2O_3 \cdot CaSO_3 \cdot 11H_2O$	-26.9 ±1.1	-7269	-8178	703.0	852.2	295
S(II)-AFm $3CaO \cdot Al_2O_3 \cdot CaS_2O_3 \cdot 13H_2O$	-30.5 ±1.1	-7795	-8782	939.1	1045.4	358
Se(VI)-AFm $3CaO \cdot Al_2O_3 \cdot CaSeO_4 \cdot 13H_2O$	-29.2 ±1.5	-7708	-8729	905.1	1335.0	352
Se(IV)-AFm $3CaO \cdot Al_2O_3 \cdot CaSeO_3 \cdot 11H_2O$	-28.4 ±0.8	-7152	-8056	727.2	877.6	337

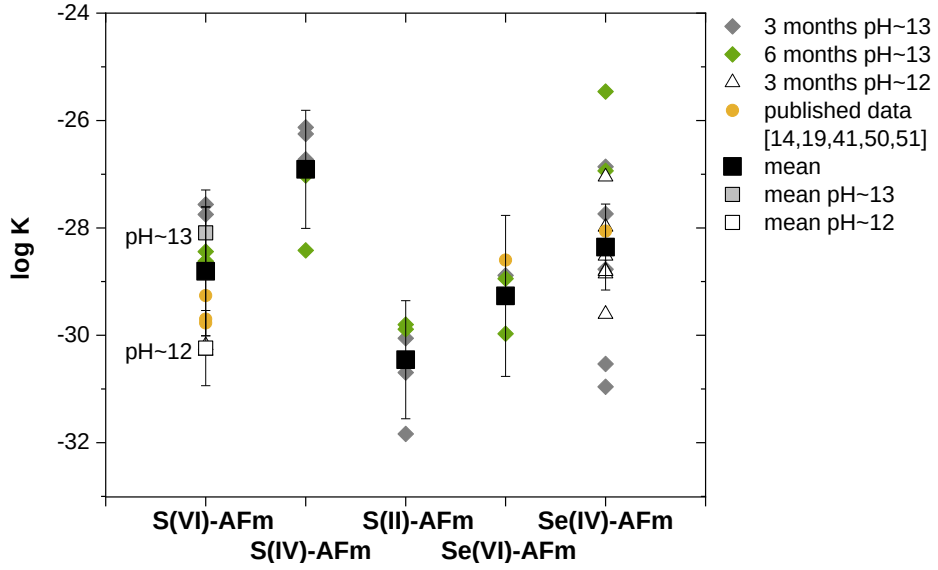

Figure 11: Solubility products of the synthesized AFm phases determined at 20°C and different equilibration time and pH. Calculated error on the mean values indicate the 95% confidence interval. Black squares represent the mean values of all measurements; for the S(VI)-AFm additionally mean values for pH~13 (light grey square) and pH~12 (white square) are shown.

4. Conclusions

The present study shows that the sulfur and selenium species S(VI), S(IV), S(II), Se(VI) and Se(IV) can be incorporated in the AFm-type phases. Such phases display the lamellar structure typical for the AFm family with trigonal or pseudo-trigonal symmetry (lowering of the symmetry observed) depending on the type of the interlayer anion and its coordination. The phases described in the hexagonal lattice are characterized by identical position of the (110) main layer reflection but different interlayer distances (00l harmonics). The latter distances depend on the size of the anion and/or the number of water molecules present in the interlayer. The attempt to refine the structure of these AFm phases was partially conclusive while it is acknowledged that more detailed investigations are needed.

The total amount of water was estimated by TGA. The number of H_2O molecules in the structure was determined to be 11 H_2O for the S(IV)- and Se(IV)-AFm, 12 H_2O for the S(VI)-AFm, and 13 H_2O for the Se(VI)- and the S(II)-AFm. The different types of structurally bound water can readily be identified by FTIR and Raman based on the position of the absorption peaks. The S(VI)-, S(II)- and Se(VI)-AFm can exist in several hydration states depending on the relative humidity of exposure.

All AFm show similar solubility products with the S(IV)-AFm being the least stable. The Se(IV)-AFm shows the largest scatter presumably as a result of its poor crystallinity. These similar solubilities suggest that high sulfur concentration in the pore solution of the cement can decrease the extent of Se binding by AFm phases.

Acknowledgements

The research leading to these results has received funding from the European Union's Horizon 2020 Research and Training Programme of the European Atomic Energy Community (EURATOM) (H2020-NFRP-2014/2015) under grant agreement n° 662147 (CEBAMA). The authors would like to thank Luigi Brunetti (Empa), Dr. Frank Winnefeld (Empa) and Dr. Mateusz Wyrzykowski (Empa) for their support in the sample characterization measurements. Dr. Erich Wieland (PSI) is greatly acknowledged for the helpful discussions and for revising the manuscript.

5. References

[1] A. Gruskovnjak, B. Lothenbach, F. Winnefeld, R. Figi, S.-C. Ko, M. Adler, U. Mäder, Hydration mechanisms of super sulphated slag cement, Cem. Concr. Res. 38 (2008), 983-992. https://doi.org/10.1016/j.cemconres.2008.03.004.

[2] B. Lothenbach, G. Le Saout, M. Ben Haha, R. Figi, E. Wieland, Hydration of low-alkali CEM III/B-SiO_2 cement (LAC), Cem. Concr. Res. 42 (2012), 410-423. https://doi.org/10.1016/j.cemconres.2011.11.008.

[3] T. Matschei, B. Lothenbach, F.P. Glasser, The AFm phase in Portland cement, Cem. Concr. Res. 37 (2007), 118-130. https://doi.org/10.1016/j.cemconres.2006.10.010.

[4] NAGRA Project Opalinus Clay. Safety report. Demonstration of disposal feasibility for spent fuel, vitrified high-level waste and long-lived intermediate level waste, Nagra Technical Report NTB 02-05 (2002), Nagra, Wettingen, Switzerland.

[5] P. Wersin, L.H. Johnson, B. Schwyn, U. Berner, E. Curti, Redox conditions in the near field of a repository for SF/HLW and ILW in Opalinus clay, Nagra Technical Report NTB 02-13 (2003), Nagra, Wettingen, Switzerland.

[6] Å. Olin, B. Noläng, E.G. Osadchii, L.-O. Öhman, E. Rosén, Chemical thermodynamics of Selenium, Elsevier, Amsterdam, 2005.

[7] H. Fischer, G. Schulz-Ekloff, D. Wöhrle, Oxidation of aqueous sulfide solutions by dioxygen. Part I: Autoxidation reaction, Chem. Eng.Technol. 20 (1997), 462-468.

[8] H. F. W. Taylor, Cement Chemistry; second ed., Thomas Telford, London, 1997.

[9] D. G. Evans & R. C. T. Slade, Structural aspects of layered double hydroxides, in: X. Duan, D. G. Evans, Layered Double Hydroxides, Ed. Springer-Verlag, Berlin, 2006, Vol. 119, 1−87.

[10] G. Renaudin & M. François, The lamellar double-hydroxide (LDH) compound with composition $3CaO{\cdot}Al_2O_3{\cdot}Ca(NO_3)_2{\cdot}10H_2O$, Acta Cryst. C55 (1999), 835-838. https://doi.org/10.1107/S0108270199003066.

[11] L. Aimoz, E. Wieland, C. Taviot-Guého, R. Dähn, M. Vespa, S.V. Churakov, Structural insight into iodide uptake by AFm phases, Environ. Sci. Technol. 46 (2012), 3874-3881. https://doi.org/10.1021/es204470e.

[12] G. Renaudin, J.P. Rapin, E. Elkaim, M. François, Polytypes and polymorphs in the related Friedel's salt $[Ca_2Al(OH)_6]^+$ $[X{\cdot}2H_2O]^-$ halide series, Cem. Concr. Res. 34 (2004), 1845-1852. https://doi.org/10.1016/j.cemconres.2004.01.003.

[13] R. Segni, N. Allali, L. Vieille, C. Taviot-Guého, F. Leroux, Hydrocalumite-type materials: 2. Local order into $Ca_2Fe(OH)_6(CrO_4^{2-})_{0.5} \cdot nH_2O$ in temperature studied by X-ray absorption and Mössbauer spectroscopies, J. Phys. Chem. Solids 67 (2006), 1043-1047. https://doi.org/10.1016/j.jpcs.2006.01.023.

[14] S.M. Leisinger, B. Lothenbach, G. Le Saout, C.A. Johnson, Thermodynamic modeling of solid solutions between monosulfate and monochromate $3CaO{\cdot}Al_2O_3{\cdot}Ca[(CrO_4)_x(SO_4)_{1-x}]{\cdot}nH_2O$, Cem. Concr. Res. 42 (2012), 158-165. https://doi.org/10.1016/j.cemconres.2011.09.005.

[15] B. Ma, A. Fernandez-Martinez, S. Grangeon, C. Tournassat, N. Findling, F. Claret, A. Koishi, N.C.M. Marty, D. Tisserand, S. Bureau, E. Salas-Colera, E. Elkaïm, C. Marini, L. Charlet, Evidence of multiple sorption modes in layered double hydroxides using Mo as structural probe, Environ. Sci. Technol. 51 (2017), 5531-5540. https://doi.org/10.1021/acs.est.7b00946.

[16] A. Mesbah, C. Cau-dit-Coumes, F. Frizon, F. Leroux, J. Ravaux, G. Renaudin, A new investigation of the Cl^--CO_3^{2-} substitution in AFm phases, J. Am. Ceram. Soc. 94 [6] (2011), 1901-1910. https://doi.org/10.1111/j.1551-2916.2010.04305.x.

[17] A. Mesbah, M. François, C. Cau-dit-Coumes, F. Frizon, Y. Filinchuk, F. Leroux, J. Ravaux, G. Renaudin, Crystal structure of Kuzel`s salt $3CaO{\cdot}Al_2O_3{\cdot}1/2CaSO_4{\cdot}1/2CaCl_2{\cdot}11H_2O$ determined by synchrotron powder diffraction, Cem. Concr. Res. 41 (2011), 504-509. https://doi.org/10.1016/j.cemconres.2011.01.015.

[18] A. Mesbah, J.P. Rapin, M. François, C. Cau-dit-Coumes, F. Frizon, F. Leroux, G. Renaudin, Crystal structures and phase transition of cementitious bi-anionic AFm-(Cl^-, CO_3^{2-}) compounds, J. Am. Ceram. Soc. 94 [1] (2011), 261-268. https://doi.org/10.1111/j.1551-2916.2010.04050.x.

[19] L. Aimoz, D.A. Kulik, E. Wieland, E. Curti, B. Lothenbach, U. Mäder, Thermodynamics of AFm-(I_2,SO_4) solid solution and of its end-members in aqueous media, Appl. Geochem. 27 (2012), 2117-2129. https://doi.org/10.1016/j.apgeochem.2012.06.006.

[20] T. Runčevski, R.E. Dinnebier, O.V. Magdysyuk, H. Pöllmann, Crystal structures of calcium hemicarboaluminate and carbonated calcium hemicarboaluminate from synchrotron powder diffraction data, Acta Cryst. B68 (2012), 493-500. https://doi.org/10.1107/S010876811203042X.

[21] I. Baur & C.A. Johnson, Sorption of selenite and selenate to cement minerals, Environ. Sci. Technol. 37 (2003), 3442-3447. https://doi.org/10.1021/es020148d.

[22] I. Bonhoure, I. Baur, E. Wieland, C.A. Johnson, A.M. Scheidegger, Uptake of Se(IV/VI) oxyanions by hardened cement paste and cement minerals: An X-ray absorption spectroscopy study, Cem. Concr. Res. 36 (2006), 91-98. https://doi.org/10.1016/j.cemconres.2005.05.003.

[23] M. Zhang, Incorporation of oxyanionic B, Cr, Mo, and Se into hydrocalumite and ettringite: Application to cementitious systems, PhD Thesis at the University of Waterloo, Ontario, Canada, 2000.

[24] H. Rojo, A.C. Scheinost, B. Lothenbach, A. Laube, E. Wieland, J. Tits, Retention of selenium by calcium aluminate hydrate (AFm) phases under strongly-reducing radioactive waste repository conditions, Dalton Transactions 00 (2018), 1-10. https://doi.org/10.1039/c7dt04824f.

[25] R. Allmann, Refinement of the hybrid layer structure $[Ca_2Al(OH)_6]^+\cdot[\frac{1}{2}SO_4\cdot 3H_2O]^-$, Neues Jb Miner. Monat. 3 (1977), 136-144.

[26] L.G. Baquerizo, T. Matschei, K.L. Scrivener, M. Saeidpour, A. Thorell, L. Wadsö, Methods to determine hydration states of minerals and cement hydrates, Cem. Concr. Res. 65 (2014), 85-95. https://doi.org/10.1016/j.cemconres.2014.07.009.

[27] L.G. Baquerizo, T. Matschei, K.L. Scrivener, M. Saeidpour, L. Wadsö, Hydration states of AFm cement phases, Cem. Concr. Res. 73 (2015), 143-157. https://doi.org/10.1016/j.cemconres.2015.02.011.

[28] H. Motzet & H. Pöllmann, Synthesis and characterization of sulfite-containing AFm phases in the system $CaO-Al_2O_3-SO_2-H_2O$, Cem. Concr. Res. 29 (1999), 1005-1011. https://doi.org/10.1016/S0008-8846(99)00082-4.

[29] D. Le Cornec, Q. Wang, L. Galoisy, G. Renaudin, L. Izoret, G. Calas, Greening effect in slag cement materials, Cem. Concr. Res. 84 (2017), 93-98. https://doi.org/10.1016/j.cemconcomp.2017.08.017.

[30] C. Vernet, Comportement de l'ion S-- au cours de l'hydratation des ciments riches en laitier (CLK). Formation de solutions solides de S-- dans les aluminates hydrates hexagonaux, Silicates Industriels 3 (1982), 85-90.

[31] I. Puigdomenech, INPUT, SED, and PREDOM: Computer programs drawing equilibrium diagrams; TRITA-OOK-3010, Royal Institute of Technology (KTH), Dept. Inorg. Chemistry, Stockholm, Sweden, 1983.

[32] H. Wanner, The NEA thermochemical data base project, Radiochim. Acta 44/45 (1988), 325–329. https://doi.org/10.1524/ract.1988.4445.2.325.

[33] M.A. Neumann, X-Cell: a novel indexing algorithm for routine tasks and difficult cases, J. Appl. Cryst. 36 (2003), 356-365.

[34] V. Favre-Nicolin & R. Černý, FOX, free objects for crystallography: a modular approach to ab initio structure determination from powder diffraction, J. Appl. Cryst. 35 (2002), 734-743. https://doi.org/10.1107/S0021889802015236.

[35] J. Rodriguez-Carvajal, PROGRAM FullProf, 2k-version 3.20, Laboratoire Léon Brillouin (CEA-CNRS), France, 2005.

[36] D.A. Kulik, T. Wagner, S.V. Dmytrieva, G. Kosakowski, F.F. Hingerl, K.V. Chudnenko, U. Berner GEM-Selektor geochemical modeling package: revised algorithm and GEMS3K numerical kernel for coupled simulation codes, Computational Geosciences 17 (2013), 1-24. https://doi.org/10.1007/s10596-012-9310-6.

[37] W. Hummel, U. Berner, E. Curti, F. J. Pearson, T. Thoenen, Nagra/PSI thermodynamic database 01/01, Universal Publisher/uPublish.com, Parkland, Florida, 2002.

[38] Y. Gu, C.H. Gammons, M.S. Bloom, A one-term extrapolation for estimating equilibrium constants of aqueous reactions at elevated temperatures, Geochem. Cosmochim. Acta 58 (1994), 3545-3560. https://doi.org/10.1016/0016-7037(94)90149-X.

[39] A. Moore & H.F.W. Taylor, Crystal structures of ettringite, Nature 218 (1968), 1048-1049. https://doi.org/10.1038/2181048a0.

[40] J.B. Champenois, A. Mesbah, C.C.D. Coumes, G. Renaudin, F. Leroux, C. Mercier, B. Revel, D. Damidot, Crystal structures of Boro-AFm and sBoro-AFt phases, Cem. Concr. Res. 42 (2012), 1362-1370. https://doi.org/10.1016/j.cemconres.2012.06.003.

[41] B. Ma, A. Fernandez-Martinez, S. Grangeon, C. Tournassat, N. Findling, S. Carrero, D. Tisserand, S. Bureau, E. Elkaïm, C. Marini, G. Aquilanti, A. Koishi, N. Marty, L. Charlet, Selenite uptake by CaAl LDH: A description of intercalated anion coordination geometries, Environ. Sci. Technol. 52 (2018), 1624-1632. https://doi.org/10.1021/acs.est.7b04644.

[42] M. Wildner & G. Giester, Crystal structures of $SrSeO_3$ and $CaSeO_3$ and their respective relationships with molybdomenite- and monazite-type compounds – an example for stereochemical equivalence of $ESeO_3$ groups (E = lone electron pair) with tetrahedral TO_4 groups, N. Jb Min., Abh. 184/1 (2007), 29-37. https://doi.org/10.1127/0077-7757/2007/0083.

[43] A. Terzis, S. Filippakis, H.J. Kuzel, H. Burzlaff, The crystal structure of $Ca_2Al(OH)_6Cl{\cdot}2H_2O$, Z. Kristallogr. 181 (1987), 29-34. https://doi.org/10.1524/zkri.1987.181.14.29.

[44] M. Francois, G. Renaudin, O. Evrard, A cementitious compound with composition $3CaO.Al_2O_3.CaCO_3.11H_2O$, Acta Cryst. C54 (1998), 1214-1217. https://doi.org/10.1107/S0108270198004223.

[45] H. Pöllmann, Die Kristallchemie der Neubildung bei Einwirkung von Schadstoffen auf hydraulische Bindelmittel, PhD Thesis at the University of Erlangen, Germany, 1984.

[46] K. Nakamoto, Infrared and Raman spectra of inorganic and coordination compounds, sixth ed., John Wiley & Sons, New Jersey, 1986.

[47] H. Siebert, Kraftkonstante und Strukturchemie. V. Struktur der Sauerstoffsäuren , Z. anorg. allg. Chemie 275 (1954), 225-240. https://doi.org/10.1002/zaac.19542750407.

[48] L. Peter & B. Meyer, Preparation and Raman spectra of thallium(I) disulfite and thallium(I) sulfite, Inorg. Chem. 24 (1985), 3071-3073. https://doi.org/10.1021/ic00213a040.

[49] G. Renaudin, R. Segni, D. Mentel, J.M. Nedelec, F. Leroux, C. Taviot-Gueho, A Raman study of the sulfated cement hydrates: ettringite and monosulfoaluminate, J. Adv. Concr. Techn. 5A (2007), 299-312. https://doi.org/10.3151/jact.5.299.

[50] T. Matschei, B. Lothenbach, F.P. Glasser, Thermodynamic properties of Portland cement hydrates in the system $CaO-Al_2O_3-SiO_2-CaSO_4-CaCO_3-H_2O$, Cem. Concr. Res. 37 (2007), 1379-1410. https://doi.org/10.1016/j.cemconres.2007.06.002.

[51] I. Baur & C.A. Johnson, The solubility of selenate-AFt ($3CaO{\cdot}Al_2O_3{\cdot}3CaSeO_3{\cdot}37.5H_2O$) and selenate-AFm ($3CaO{\cdot}Al_2O_3{\cdot}CaSeO_4{\cdot}xH_2O$), Cem. Concr. Res. 33 (2003), 1741-1748. https://doi.org/10.1016/S0008-8846(03)00151-0.

6. Appendix

A.1: Measured IC concentrations, pH and solubility products for the S-AFm phases at 20°C.

	Al	Ca	Na	SO_4	SO_3	S_2O_3	pH	$[OH^-]$	Log K
	[mmol/l]	[mmol/l]	[mmol/l]	[mmol/l]	[mmol/l]	[mmol/l]		[mmol]	
sulfate: S(VI)									
3 months; pH~13									
#1	7.21	0.642	206.5	1.22*			13.2	0.161	-27.75
#2	13.74	0.551	229.6	3.67			13.1	0.137	-27.56
6 months; pH 13									
#1	4.47	0.646	216.2	1.35			13.1	0.137	-28.62
#2	2.64	0.902	211.0	1.50			13.1	0.125	-28.44
*3 months; pH~*12									
#1	1.41	6.28	0.565	<.052			12.1	0.012	-30.19
#2	0.551	5.73	0.548	<.052			12.2	0.016	-30.29

sulfite: S(IV)								
3 months; pH~13								
#1	14.46	0.616	207.1	6.40*		13.2	0.132	-26.72
#2	16.13	0.664	205.9	7.92*		13.3	0.189	-26.13
#3	15.56	0.640	206.6	8.02*		13.3	0.174	-26.25
6 months; pH~13								
#1	14.48	0.623	224.3	7.13*		13.1	0.122	-27.02
#2	2.38	0.732	211.6	4.41*		13.1	0.116	-28.42
thiosulfate: S(II)								
3 months; pH~13								
#1	0.056	3.29	172.5		<.045	13.2	0.141	-30.62
#2	0.395	1.66	162.4		0.100	13.0	0.107	-30.05
#3	0.066	2.48	179.4		0.016	13.1	0.117	-31.84
6 months; pH~13								
#1	0.268	3.15	176.0		0.026	13.1	0.112	-29.89
#2	0.296	3.18	172.7		0.028	13.0	0.107	-29.80

* values corrected for sulfite oxidation.

A.2: Measured IC concentrations, pH and solubility products for the Se-AFm phases at 20°C.

	Al	Ca	Na	SeO_4	SeO_3	pH	$[OH^-]$	Log K
	[mmol/l]	[mmol/l]	[mmol/l]	[mmol/l]	[mmol/l]		[mmol]	
selenate: Se(VI)								

3 months; pH~13								
#1	0.242	3.02	169.0	0.169		13.2	0.137	-28.88
6 months; pH~13								
#1	0.220	1.88	189.6	0.291		13.1	0.122	-29.97
#2	0.266	2.98	188.2	0.339		13.1	0.112	-28.94
selenite: Se(IV)								
3 months; pH~13								
#1	20.24	0.842	225.6		0.498	13.2	0.155	-26.86
#2	7.81	0.526	154.8		0.257	13.0	0.091	-28.48
#3	5.25	0.619	156.7		0.161	13.0	0.103	-27.74
#4	5.08	0.181	152.4		0.253	13.0	0.099	-30.96
#5	15.92	0.657	205.7		0.590	13.2	0.154	-28.77
#6	14.36	0.289	154.9		0.221	13.0	0.099	-30.53
6 months; pH~13								
#1	16.63	0.300	228.5		0.676	13.1	0.127	-25.46
#2	19.99	0.880	240.0		1.01	13.1	0.121	-26.94
*3 months; pH~*12								
#1	2.59	7.50	0.423		0.080	12.3	0.017	-27.05
#2	3.72	6.67	0.420		0.012	12.0	0.009	-28.52
#3	0.103	7.34	1.73		0.305	12.4	0.027	-28.85
#4	3.12	6.99	1.71		0.004	12.1	0.012	-28.80
#5	2.65	7.16	1.83		0.001	12.3	0.021	-28.81
#6	0.125	7.44	1.76		0.139	12.2	0.015	-29.60
#7	2.58	7.91	0.394		0.013	12.2	0.015	-27.98